

## Spatial decay of energy density of tidal internal waves

Iossif D. Lozovatsky<sup>1</sup>

Environmental Fluid Dynamics Program, Department of Mechanical and Aerospace Engineering, Arizona State University, Tempe, Arizona, USA

Eugene G. Morozov

P. P. Shirshov Institute of Oceanology, Russian Academy of Sciences, Moscow, Russia

H. J. S. Fernando

Environmental Fluid Dynamics Program, Department of Mechanical and Aerospace Engineering, Arizona State University, Tempe, Arizona, USA

Received 12 October 2001; revised 25 February 2003; accepted 17 March 2003; published 25 June 2003.

[1] The spatial decay of energy density of tidal internal waves (TIW) was studied using field data taken in the Indian Ocean near the Mascarene Ridge and in the Canary Basin of the eastern Atlantic near the Heyres-Irving-Cruiser chain of seamounts. Several moorings were deployed at distances between 90 and 1745 km east of these topographic features, with instruments located in the depth range 500–2500 m. The energy densities of TIW averaged over the spring-neap cycle were calculated using semidiurnal tidal components of current and temperature time series as well as local vertical gradients of temperature and density. It was found that the horizontal component of TIW,  $E_H$ , is less depth-dependent compared to the vertical component,  $E_V$ , although both components showed a general decrease of magnitude with the distance from topography. The decrease of total energy density  $E_{TW} = E_H + E_V$  with distance from the topography is more rapid than that assumed in the work of Morozov [1995], and followed an inverse power law. At a distance of about  $x \approx 10\lambda$  from the topography (where  $\lambda$  is the wavelength of the first mode),  $E_{TW}$  in the main thermocline becomes equal to the energy density of the forcing barotropic tide, whereas for  $x/\lambda < 2$ ,  $E_{TW}$  exceeds the energy of the entire range of internal waves of the Garrett-Munk spectrum. A nonhydrostatic, nonlinear, two-dimensional numerical model shows a reasonable agreement with the observations for  $x/\lambda < 2-3$ , but in the far field it predicts a faster spatial decay of  $E_{TW}$  than observed, possibly because of topographic generation of TIW along the measurement swath. The turbulent diffusivity estimates based on the McComas and Muller [1981] model exceeded  $10^{-4} \text{ m}^2/\text{s}$  within the main pycnocline at  $x = 100 \text{ km}$  and suggest mixing enhancements due to TIW up to distances of 1000 km from the topography. *INDEX TERMS*: 4544 Oceanography: Physical: Internal and inertial waves; 4255 Oceanography: General: Numerical modeling; 9340 Information Related to Geographic Region: Indian Ocean; 9325 Information Related to Geographic Region: Atlantic Ocean; *KEYWORDS*: internal tides, mixing, diffusivities, submarine ridges, seamounts

**Citation:** Lozovatsky, I. D., E. G. Morozov, and H. J. S. Fernando, Spatial decay of energy density of tidal internal waves, *J. Geophys. Res.*, 108(C6), 3201, doi:10.1029/2001JC001169, 2003.

### 1. Introduction

[2] Tidal mixing is an important process that influences mass and heat balances in the ocean [Sjoberg and Stigebrant, 1992; Morozov, 1995; Munk and Wunsch, 1998]. Tidal internal waves (TIW) generated over steep topographic features degenerate in time and space to small-scale motions consisting of turbulence and high-frequency short

nonlinear waves. Baroclinic energy density increases significantly near the sources of TIW. At the Malin shelf break (located at the northwestern coast of British Islands), for example, the tidal energy density reaches  $6.0 \text{ J/m}^3$  [Inall *et al.*, 2000]. Thorpe [1999] suggested that a considerable part of the internal wave energy dissipates near the source. Internal tides, however, travel far from the source region (e.g., slopes) while losing energy during the propagation. For example, according to the acoustic measurements of Dushaw *et al.* [1995], TIW generated near the Hawaiian Ridge propagate over 2000 km from the source. Holloway and Merrifield [1999] used a numerical model to calculate the decay of TIW energy generated over seamounts and submarine ridges, with application to the Hawaiian Ridge.

<sup>1</sup>Also at P. P. Shirshov Institute of Oceanology, Russian Academy of Sciences, Moscow, Russia.

They found the barotropic flow to go around isolated topographic features, rather than over it, thus producing only a weak internal tide. On the other hand, barotropic tides flow over long submarine ridges, generating energetic baroclinic tidal waves of which the energy content is determined by the barotropic tidal velocity and the ridge geometry. Most intense internal tides are generated when their characteristics are parallel to the topographic slope at the depth of maximum stratification [New, 1988]. An archipelago of seamounts, separated by deep troughs, when oriented normally to the propagation of barotropic tide, also may trigger TIW with energy densities comparable to those of long ridges [Merrifield *et al.*, 2001]. Also, the spatial redistribution of energy in these two cases can be quite different. The work reported herein is focused on the distribution of TIW energy away from an energetic source, with emphasis on the Mascarene Ridge in the Indian Ocean. The vertical isopycnal displacements for this case have been addressed by Morozov and Vlasenko [1996], but the associated energetics has not been analyzed. We calculated, for the first time to our knowledge, the energy density east of the Mascarene Ridge using field data and a numerical model. The results are compared with similar observations taken east of the Heyres-Irving-Cruiser chain of seamounts in the Canary Basin (eastern Atlantic). Morozov [1995] roughly estimated a 5% decrease of TIW amplitude over one wavelength, corresponding to a 10% decrease of TIW energy. This assessment requires a detailed examination, which is undertaken in the present study.

[3] The field measurements and the limitations of the data collected are discussed in section 2. In section 3, we describe basic properties of tidal fields and background hydrology of regions in point. Data processing procedures, the energy density  $E_{TW}$  of TIW, and its spatial variations are discussed in section 4.1. The role of TIW is assessed in section 4.2 by comparing  $E_{TW}$  with the background Garrett-Munk (GM) internal wave field and the energy of the barotropic tide. A comparison of TIW measurements with numerical calculations is given in section 5. In section 6, following Wijesekera *et al.* [1993] and Polzin *et al.* [1995], McComas and Muller's [1981] model is applied to estimate the spatial distribution of vertical diffusivities associated with the TIW field. A summary of the results is presented in section 7.

## 2. Observational Program

[4] Located in an area of energetic barotropic tides, the Mascarene Ridge is characterized by mountains with flat summits straddled by channels. Some of the summits are only 50 m below the sea surface whereas the channels can be more than 1000 m deep. To calculate the TIW energy at various distances from the ridge, the mooring measurements taken east of the Mascarene Ridge [Morozov and Vlasenko, 1996] were utilized. A cluster of six moorings was centered at 13.5°S, 62°E (Figure 1a, circles). The distances to the moorings from the ridge, in the direction normal to the calculated wave fronts generated at the ridge, were 90, 140, 185, 230, 245, and 285 km. The data were collected from six instruments at each station, at depths of 500, 700, 1000, 1200, 1800, and 2500 m. The current and temperature time

records were obtained using the POTOK instrument [Kontar and Sokov, 1994] (see Appendix A for details). The mooring measurements were complemented by CTD profiling near the central buoy.

[5] The mooring measurements were taken over 16 days, equivalent to 30 semidiurnal periods and covering a complete spring-neap cycle. Thus the averaging of squared tidal amplitudes over this period is expected to give confident estimates of the amplitudes and energy of TIW. The relative shortness of the observational period, however, is a drawback. The data so obtained can be considered a snapshot of the distribution of TIW energy density at various depths and distances from the ridge. Analyses of rms TIW amplitude and energy (see the discussion following Figure 6 in section 4.1) showed that sufficiently reliable estimates can be obtained if averaging periods over 350 hours are used. This corresponds to the duration of measurements near the Mascarene Ridge (section 4). The study also included two long-term moorings (5 months in 1995–1996) deployed at distances 1100 and 1745 km east of the Mascarene Ridge (Figure 1a, squares), with instruments at the depths of 500 and 1200 m [Morozov *et al.*, 1999]. Surface (near zone) and subsurface (far zone) floats were used for the deployment of moorings.

[6] The measurements in the Atlantic, east of the Heyres-Irving-Cruiser seamounts were taken in October–November 1989. These seamounts have flat summits about 300 m below the sea surface and steep flanks down to 4000 m depth; the depth of the seafloor gradually increases to 5200 m thereafter. A cluster of five moorings with instruments at 700, 900, 1000, and 1200 m was located southeast of the seamount chain at distances 145–225 km from the 400-m isobaths located along the slopes of seamounts (Figure 1b). A CTD survey also was conducted during this 30-day mooring operation.

[7] Technical details of the POTOK instrument and a critical discussion on surface and subsurface floats are given in Appendix A. The measurements in both regions were carried out under calm and moderate winds; therefore mooring measurements with surface floats were not contaminated by high winds and rough seas.

## 3. Background Characteristics of TIW

[8] The mean stratification in the depth range 500–1700 m east of the Mascarene Ridge is swayed by sub-Antarctic and Arabian-Red Sea waters, while 1700–4000 m depths are dominated by Indian Ocean Central Water. The hydrographic regime of the Canary Basin east of the seamount chain depends on the interaction between Intermediate Atlantic Water mass (the depth range 200–1500 m) and Mediterranean Water, with a core at 1000–1200 m.

[9] The characteristics of TIW in this region can be studied via normal wave modes in an idealized configuration, having a flat bottom and zero forcing beyond the slopes of the topographic feature. The wavelength of TIW can be estimated (numerically) from the dispersion relation based on the equation for vertical velocity ( $w$ ) of internal waves; this in turn, can be compared with wavelengths obtained from mooring data. To this end, the equation for the amplitude of the vertical velocity  $W(z)$  at the semidiurnal

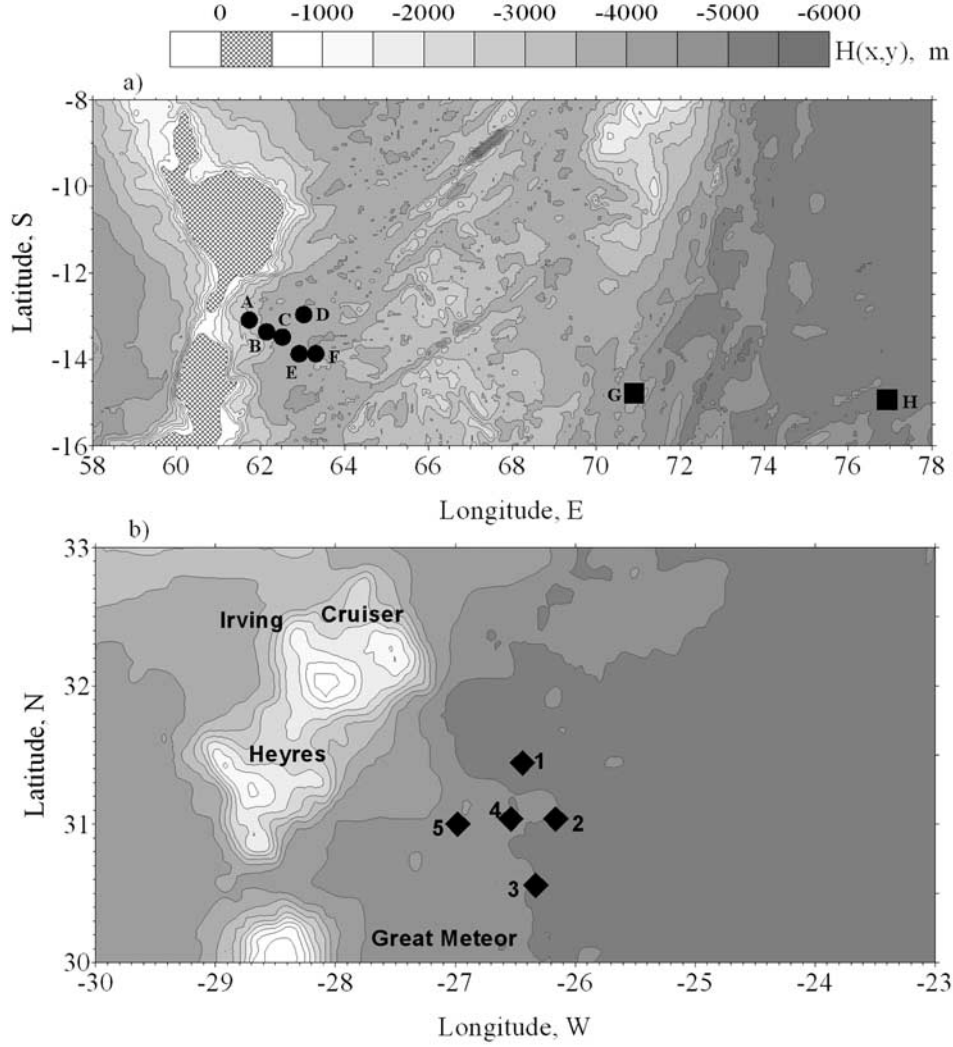


**Figure 1.** (a) Mooring arrays near the Mascarene Ridge in the Indian Ocean and (b) the chain of the Heyres-Irving-Cruiser seamounts in the Canary Basin of the eastern Atlantic.

frequency  $\omega_T = 2\pi/\tau_T$  in the water column with the depth-dependent buoyancy frequency  $N(z)$ ,

$$\frac{d^2W}{dz^2} + \frac{N^2(z)}{g} \frac{dW}{dz} + \frac{(N(z)^2 - \omega_T^2)}{(\omega_T^2 - f^2)} \kappa^2 W = 0, \quad (1)$$

where  $\tau_T = 12.4$  hours is the M2 tidal period,  $f$  is the Coriolis parameter, and  $g$  is the gravity, was used to calculate the normal modes of the internal tide with  $W = 0$  at the bottom and at the sea surface. The  $W(z)$  and  $U(z) = -(dW/dz)/\kappa$  profiles for the first mode are shown in Figure 2, along with the averaged profiles of  $N(z)$  for the Mascarene and Canary Basin regions. The wavelengths  $\lambda_T = 2\pi/\kappa_T$  of the first mode are given in Table 1 as the function of ocean depth  $H$ ; here equation (1) was numerically integrated by assuming that  $N(z)$  is constant below 3500 m in the Indian Ocean and 5000 m in the Atlantic Ocean, respectively. Note that  $\lambda$  increases only slightly with  $H$ .

[10] The direction of the tidal wave propagation can be deduced from the spatiotemporal spectra at the semidiurnal

frequency. At semidiurnal frequency  $f_T = \omega_T/2\pi$ , the spectra were calculated using the following formula of Barber [1963]:

$$S(k_x, k_y, f_T) = 2 \sum_{i=1}^{n-1} \sum_{j=i+1}^n [P_{ij}(f_T) \cos 2\pi(k_x x_{ij} + k_y y_{ij}) - Q_{ij}(f_T) \cdot \sin 2\pi(k_x x_{ij} + k_y y_{ij})], \quad (2)$$

where  $k_x$  and  $k_y$  are the components of horizontal wave numbers  $k^2 = k_x^2 + k_y^2$ ;  $i$  and  $j$  are the mooring indices,  $n$  is the total number of moorings;  $P_{ij}$  and  $Q_{ij}$  are the real and imaginary parts of the cross spectrum between moorings with numbers  $i$  and  $j$ ;  $x_{ij} = X_i - X_j$  and  $y_{ij} = Y_i - Y_j$  are the projections of the distances between the moorings on the horizontal axes  $x$  and  $y$ . This method accounts for statistical phase difference between pairs of records. The cross spectra were calculated for each pair of records (for possible combinations) using Fourier transformation of cross-correlation functions with Hamming window and 20 degrees of

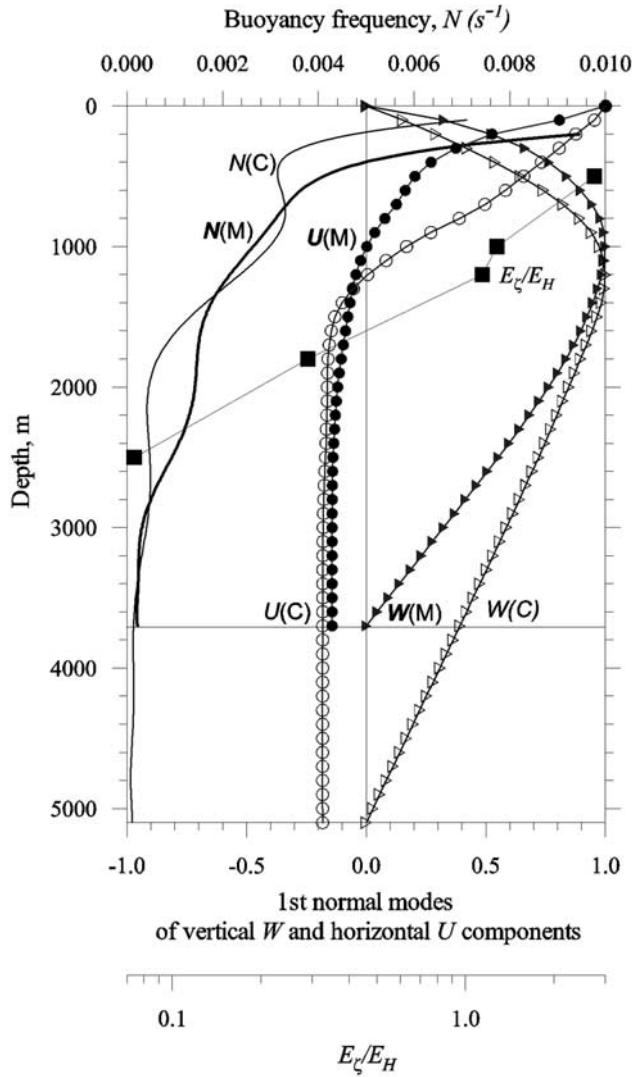


**Figure 2.** Polynomial fitted buoyancy frequency profiles (denoted by  $N$ ) and normalized eigen functions of the first vertical ( $W$ ) and horizontal ( $U$ ) TIW modes for the Mascarene region (M) and Canary Basin (C). The mean ratio between vertical  $E_z$  and horizontal  $E_H$  components of the TIW energy density near the Mascarene Ridge is shown by squares.

freedom. We used the temperature mooring records, which register vertical motion induced by internal waves in stratified layers. The resolution of spectral estimates depends on the number of moorings, their separation, and the length of records. The distances between the moorings must be shorter than half the TIW wavelength, and the array ought to be large enough to resolve the horizontal scale of TIW. The interpretation of phase differences is uncertain, if the distance between moorings is too large.

[11] The spectra were calculated with fine resolution over  $k$ ,  $\Delta k = 0.5 \times 10^{-6}$  cpm in both directions, ensuring smooth cross-sectional spectral contours shown in Figure 3 for temperature fluctuations at semidiurnal frequency. The spectra were cut off at  $k_x$  and  $k_y$ , exceeding  $\pm 0.125 \times 10^{-4}$  cpm because the wavelengths lower than 80 km cannot be resolved due to relatively large distances between

the moorings. The position of the spectral maximum at  $k_x = 6.5 \times 10^{-6}$  and  $k_y = -2.5 \times 10^{-6}$  cpm (Figure 3a) signifies a wavelength of  $\lambda = 144$  km, which is in agreement with the wavelength of the first mode presented in Table 1. Internal tide propagates from the Mascarene Ridge in the southeastern direction with an azimuth of  $110^\circ$ . For the Heyres-Irving-Cruiser seamounts, the spectral maximum is at  $k_x = 7 \times 10^{-6}$  and  $k_y = -3 \times 10^{-6}$  cpm, corresponding to the first mode with  $\lambda = 131$  km, propagating in the southeastern direction with an azimuth of  $113^\circ$  (Figure 3b). The wavelength estimates from the spectral analysis and the calculation of eigen functions agreed within  $\pm 10\%$ . Accordingly, we assigned  $\lambda = 145$  km for the Indian Ocean and  $\lambda = 125$  km for the Atlantic Ocean for normalization purposes. The above estimates are valid for a planar wave front, which is only a rough approximation for the closest moorings because of significant irregularities along the topography. In both regions, the distances from the ridges to the moorings are measured from the 400 m isobath.

## 4. Observations of Energy Densities of Internal and Barotropic Tidal Waves

### 4.1. Data Processing

[12] The energy densities of internal ( $E_{TW}$ ) and barotropic ( $E_{BT}$ ) tides averaged over a wave period were calculated as [Torggrimson and Hickey, 1979; Holloway and Merrifield, 1999]:

$$E_{TW}(z) = 0.25\rho\left(\overline{u_{IT}^2(z)} + \overline{v_{IT}^2(z)} + N^2(z)\overline{\varsigma_{IT}^2(z)}\right) \quad (\text{internal tide}) \quad (3)$$

and

$$E_{BT} = 0.25\rho_0[H(U_B^2 + V_B^2) + g\eta^2]/H \quad (\text{barotropic tide}), \quad (4)$$

where the amplitudes of the semidiurnal internal tidal components are  $u_{IT}$ ,  $v_{IT}$  (zonal and meridional currents), and  $\varsigma_{IT}$  (vertical displacements);  $U_B$ ,  $V_B$ , and  $\eta$  are the amplitudes of currents and surface elevation of the M2 barotropic tide, respectively;  $\rho$  is the depth-dependent water density with a mean  $\rho_0$  in the ocean of depth  $H$ .

**Table 1.** Wavelengths  $\lambda$  of the First Internal Mode of the Semidiurnal Tide Calculated for Various Bottom Depths  $H$  Near the Mascarene Ridge and Heyres-Irving-Cruiser Seamount

$H$ , m	$\lambda$ , km
<i>Indian Ocean, East of the Mascarene Ridge</i>	
3500	140.4
3600	141.1
3700	141.7
3800	142.4
3900	143.0
4000	143.6
<i>Atlantic Ocean, East of the Chain of Seamounts Heyres-Irving-Cruiser</i>	
5000	120.1
5100	120.4
5200	120.7
5300	121.1
5400	121.3
5500	121.6
5000	120.1

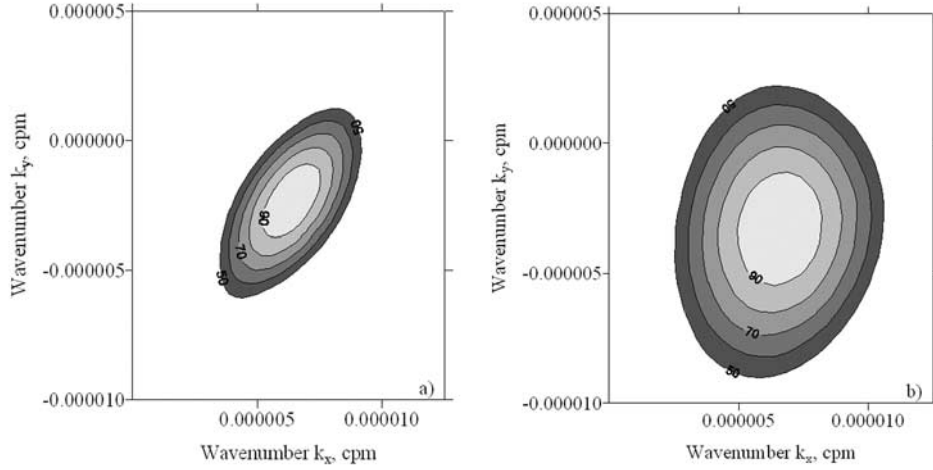


**Figure 3.** Contour plots of spatiotemporal temperature spectra at the semidiurnal frequency for the moorings located southeast of (a) Mascarene Ridge,  $z = 1200$  m, and (b) seamounts Heyres-Irving-Cruiser,  $z = 1000$  m. The contours are marked as a percentage of the principal maximum located at focal point, which identifies the direction of semidiurnal internal tide propagation. The wave number obtained corresponds to the first mode of internal tide generated at the topography. The spectra are shown only for positive  $k_x$  because there are no statistically significant spectral amplitudes at  $k_x < 0$ .

[13] The barotropic energy for the Mascarene region is mapped in Figure 4. These calculations were made by S. Erofeeva using the OSU tidal data inversion software (OTIS) [Egbert and Erofeeva, 2002], which is based on an inverse model [Egbert, 1997] with TOPEX/POSEIDON satellite data assimilation. The barotropic tide away from the ridge has a velocity of 1–2 cm/s. In the proximity of the ridge, the velocity exceeds 40 cm/s. Figure 4 underscores the role of bottom topography in the spatial distribution of energy of barotropic tide at various distances from the ridge (compare with Figure 1a). Because the energy flux of

barotropic tide is approximately constant in the course of tidal propagation, the energy density increases in shallow regions (e.g., over a ridge).

[14] The density of the horizontal-component of TIW kinetic energy was determined by the sum of squared velocity amplitudes in equation (2),  $E_H(z) = 0.25\rho(u_{IT}^2(z) + v_{IT}^2(z))$ , while the energy density of vertical displacements  $E_c$  was evaluated as  $E_c = 0.25\rho N^2 \zeta_{IT}^2(z)$ . In order to estimate the energy density of TIW, we subtracted the energy of barotropic currents  $E_{BTC} = 0.25 \rho_o(U_B^2 + V_B^2)$  from  $E_{Hm}(z) = 0.25\rho(u_{ITm}^2(z) + v_{ITm}^2(z))$ , where  $E_{Hm}$  is

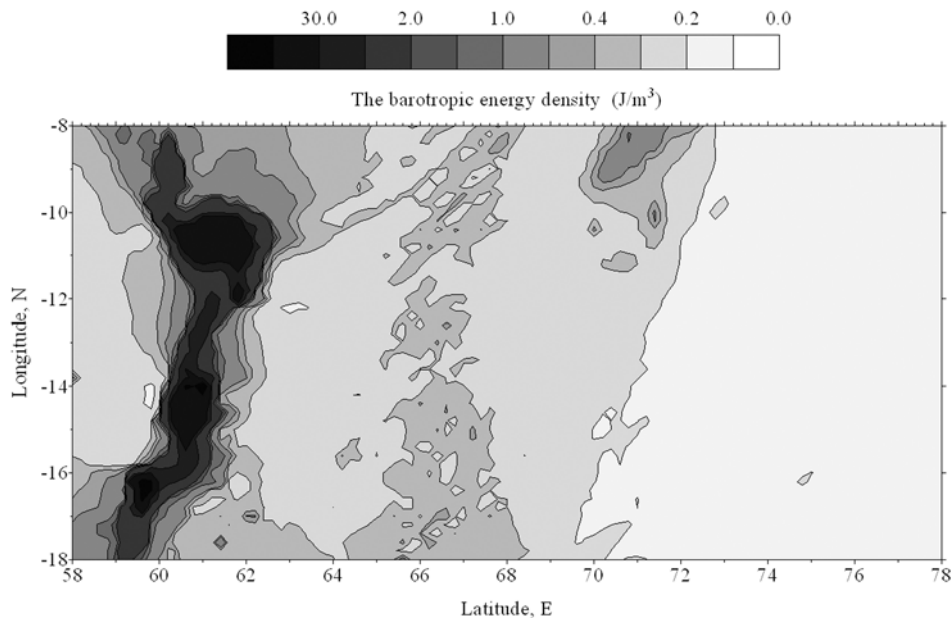


**Figure 4.** Energy density of the M2 barotropic tide near the Mascarene Ridge. The contours reflect the bottom relief, showing significant enhancement of the barotropic tidal energy density at the ridge.

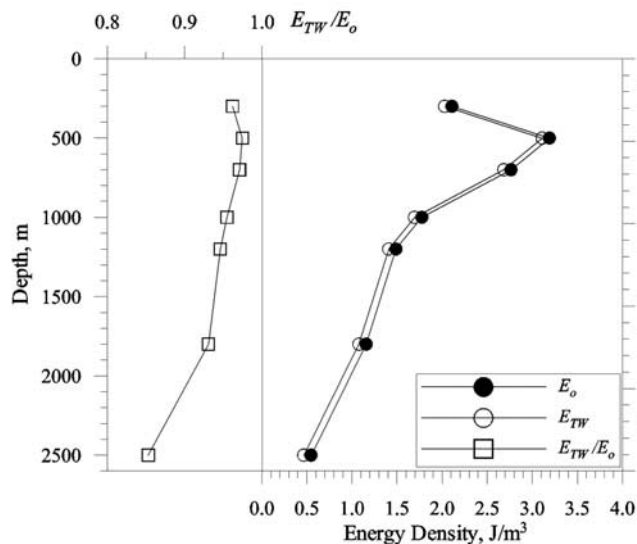


**Figure 5.** Energy density of tidal internal waves  $E_{TW}$  and total energy (internal plus barotropic tide) density  $E_0$  at the M2 frequency at  $x = 285$  km from (left) the Mascarene Ridge and (right) the ratio  $E_{TW}/E_0$ .

the total measured horizontal energy density calculated based on the semidiurnal tidal components  $u_{Tm}$  and  $v_{Tm}$  obtained from mooring current series. To demodulate semidiurnal tidal components from the current and temperature time series, an elliptic band-pass filtering was used (see section A3 in Appendix A for details). The residual  $E_H = E_{Hm} - E_{BTC}$  represents the horizontal component of the baroclinic tidal energy density and the sum  $E_H + E_\zeta = E_{TW}$  is the total energy density of TIW. A comparison between the energy density of TIW,  $E_{TW}$ , and total energy density at the semidiurnal frequency  $E_0 = E_{Hm} + E_\zeta$  is given in Figure 5 for the mooring located at 285 km from the Mascarene Ridge. The ratio  $E_{TW}/E_0$  shows that the contribution of TIW to the total energy at  $\omega = (2\pi/12.4)$  per hour varies from 0.97 in the depth range 500–1000 m to 0.85 at 2500 m. The energy of TIW decreases from a maximum in the main pycnocline ( $E_{TW} = 3.1 \text{ J/m}^3$  at  $z = 500$  m in this particular case) toward the sea surface and the ocean floor.

[15] The variability of TIW amplitude, induced due to the spring-neap cycle, posed a problem for selecting a suitable averaging period for obtaining reasonable estimates for  $E_{TW}$ . Averaging over at least one such cycle was mandatory, although longer records increase statistical reliability of estimates. To determine the shortest averaging period that guarantees stable estimates of  $E_{TW}$ , varying averaging time intervals  $\tau$  containing high and low TIW amplitudes were used and the results are shown in Figure 6; averaging over periods with  $\tau > 300$  hours appears to be the best.

[16] The highest TIW amplitudes, which occur mostly during the spring tide, are expected to provide stable estimates for “extreme” energy densities, even when one or two spring periods are considered. These extreme TIW events provide valuable information on largest propagation distances (and associated diapycnal mixing) of excess tidal energy generated near topography. Assuming internal wave displacements and current components as random variables  $y$ , we calculated cumulative distribution functions  $F(y)$  to

identify extreme TIW amplitudes in every demodulated record using a threshold level of probability. This could be, for example,  $F(y_0) = F_0 = 0.67$ , for the normal distribution, corresponding to  $y_0 = \langle y \rangle + \text{rms}(y)$ , where  $\langle y \rangle$  and  $\text{rms}(y)$  are the mean and root mean square values. For the Weibull distribution [Weibull, 1951], which is commonly used to describe the probability of life lengths,  $F_0 = 0.632$  quantifies the scale parameter  $b_W$  of the distribution, known in technical applications as a characteristic life length. Lozovatsky and Erofeev [1993] showed that the Weibull distribution could be successfully used as a statistical model for fine structure inhomogeneities of squared buoyancy frequency in oceanic pycnocline. As evident from Figure 7, TIW amplitudes of temperature and current records obtained near the Mascarene Ridge can be well approximated by the Weibull distribution. Therefore we imposed the following condition to identify extreme amplitudes from filtered records of 350 hours:  $y > y_0$  ( $F_y > F_0 = 0.632$ ) where  $F_y$  is the empirical Weibull cumulative function. The random variable  $y$  represents squared amplitudes of either  $A_u^2$ ,  $A_v^2$ , or  $A_T^2$  and  $y_0$  corresponds to  $F_0 = 0.632$ . The estimates of extreme TIW energies were averaged over the total length of mooring records.

#### 4.2. Data Analysis

[17] Between 90 and 1745 km from the Mascarene Ridge, the averaged TIW amplitudes in the main thermocline decreased from 40 to 3 m. The highest energy densities of vertical displacements  $E_\zeta$  were observed at  $z = 500$  m (Figure 8a). Near the ridge ( $x/\lambda = 0.62$ , where  $\lambda = 145$  km), in the depth range, where the first mode of the vertical velocity has a maximum shown in Figure 2,  $E_\zeta = 2.7 \text{ J/m}^3$  at  $z = 1000$  m. At a distance of  $x/\lambda = 7.6$  from the ridge,  $E_\zeta$  reduced by a factor of 16 ( $0.16 \text{ J/m}^3$  at  $z = 1200$  m).

[18] The eigen functions for the first mode of horizontal velocities of internal tides depict minimum values in the depth range 1000–1200 m, which may explain why the smallest densities of horizontal kinetic energy  $E_H$  deduced from the current measurements in Figure 8b are localized at the depths  $\sim 1200$  m. Within the main thermocline (between 500 and 2500 m), the horizontal and vertical energy densities decrease by a factor of approximately 10 over a distance of 7 wavelengths ( $x/\lambda = 0.6\text{--}7.6$ ).

[19] As evident from Figure 8, at all distances from the topography,  $E_H$  is less depth-dependent than  $E_\zeta$ . On the

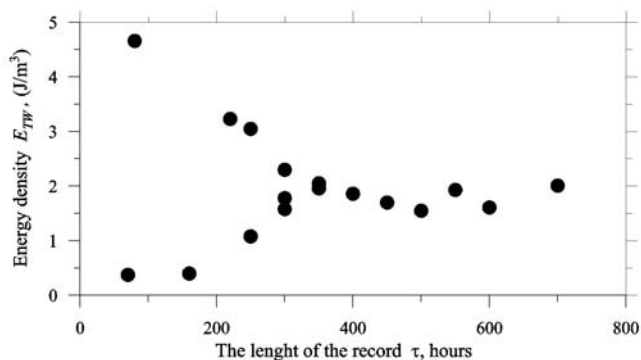


**Figure 6.** An example of the dependence of TIW energy density on the averaging length  $\tau$ . Atlantic Ocean, mooring 1,  $z = 900$  m.

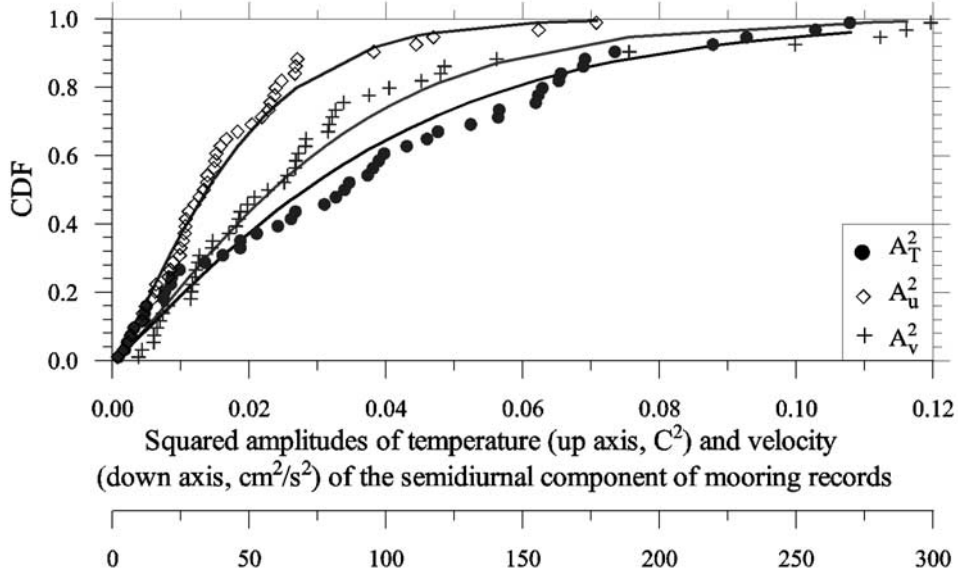


**Figure 7.** Cumulative distributions (CDF) of the squared amplitude of TIW temperature  $A_T^2$  and velocity components ( $A_u^2, A_v^2$ ) approximated by the Weibull probability function (the Mascarene Ridge,  $z = 1000$  m).

other hand, in the near field of the ridge,  $x/\lambda = 0.6-2$ , the ratio  $E_c/E_H$  strongly depends on the depth, without noticeable spatial variability. The mean values of  $E_c/E_H$  in the near zone are given in Figure 2 at  $z = 500, 1000, 1200, 1800$ , and  $2500$  m, where data are available at least from five moorings. Since rms of  $E_c/E_H$  at various depths are almost the same, (close to 50% of the mean), the gradual decrease in the mean ratio  $E_c/E_H$  from 2.8 at  $z = 500$  m down to 0.07 at  $z = 2500$  m is statistically significant. If we exclude the mooring closest to the ridge where the wave amplitudes reach 36–44 m, the mean vertical displacements  $\langle \zeta_T \rangle$  at the rest of the five moorings ( $0.6 < x/\lambda < 2$ ) have almost constant values  $\langle \zeta_T \rangle = 21-23$  m in the depth range of 500–1800 m, which is not fully consistent with eigen functions  $W(z)$  of linear waves given in Figure 2. At 2500 m, the mean amplitudes of vertical displacements  $\langle \zeta_T \rangle$  reduce to 13.7 m at all moorings. The significant drop of  $E_c/E_H$  with depth can be attributed to continuous decrease of  $W(z)$  and the mean buoyancy frequency  $N(z)$  below 1000 m, which reduce  $E_c$ . On the other hand, the almost constant horizontal component  $U(z)$  suggests a low variation of  $E_H$ .

[20] The total energy  $E_{TW}$  evolution shown in Figure 8c indicates that internal tide is losing about half of its energy propagating over each wavelength of the first mode. The energy density of the M2 and S2 constituents of the barotropic tide shown in Figure 9 is also decreasing in the near zone, following the increase of the bottom depth. Beyond 250 km from the ridge, however, the energy density of the barotropic tide is small and remains almost constant, while the decrease in baroclinic energy continues. At  $x/\lambda = 12$  ( $x = 1745$  km),  $E_{TW}$  is 10 times smaller than that at  $x/\lambda = 2$  ( $x = 250$  km).

[21] Internal tide is generated due to the interaction of barotropic tide with topography. The ratio of energy densities between the baroclinic and barotropic tides is given in Figure 10. The data can be approximated by an exponential function shown in the figure, suggesting that closer to the ridge ( $x/\lambda = 0.6$ ) the energy of the semidiurnal internal tide is one order of magnitude larger than the forcing barotropic

tide. The ratio  $E_{TW}/E_{BT}$  falls below 1 at  $x/\lambda > 10$ , indicating that the vertical displacements induced by tidal internal wave are insignificantly small therein.

[22] To compare the energy of the internal tide with that of the background internal wave field in the region, the ratio  $E_{TW}/E_{GM}$ , where  $E_{GM}$  is given by the Garrett-Munk model [Munk, 1981]

$$E_{GM} = \rho b^2 N_0 N E, \quad (5)$$

was calculated (see Figure 11). Here the parameters for the GM model are  $b = 1.3$  km,  $E = 6.3 \times 10^{-5}$ ,  $N_0 = 5.3 \times 10^{-3}/s$ , and  $N(z)$  is the local buoyancy frequency. Note that  $E_{GM}$  signifies oceanic internal wave climatology in the frequency range between  $N$  and  $f$ , excluding TIW. Note that individual samples belonging to different depths of a given mooring collapse better, as compared to their dimensional counterparts shown in Figure 8c. The estimates of  $E_{TW}/E_{GM}$  can be best approximated within  $0.6 < x/\lambda < 12$  by a power law

$$E_{TW}/E_{GM} = 2.2 \times (x/\lambda)^{-1.2}, \quad (6)$$

which is represented in Figure 11 by line (a) with a coefficient of determination  $r^2 = 0.91$ .

[23] The insert in Figure 11 shows Mascarene region data plotted with those taken from Atlantic moorings. The best fit at this panel for the combined data set, indicates a power law similar to equation (6). Note that the Atlantic data are available only for  $z = 700, 900$ , and  $1000$  m in a narrow range  $1 < x/\lambda < 2$ . Therefore we have only used Mascarene measurements at 700 and 1000 m depths ( $x/\lambda < 2$ ) for comparison.

[24] According to equation (6),  $E_{TW}/E_{GM} = 1$  at  $x/\lambda \approx 1.9$ , which means that within  $\sim 2\lambda$  from the topography the energy of TIW exceeds the canonical GM level (equation (5)). At the distance  $x/\lambda = 7.5$  (about 1000 km from the Mascarene Ridge), TIW still contribute additional 20% to

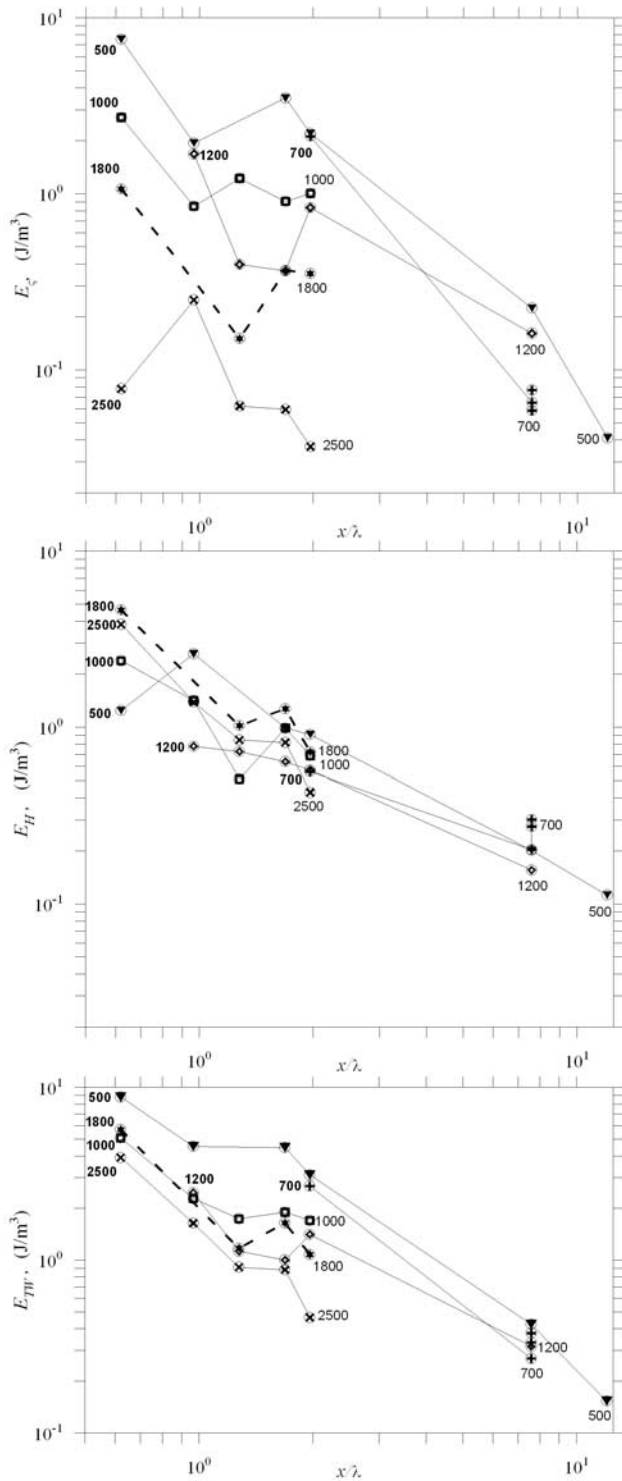


**Figure 8.** Vertical  $E_C$  and horizontal  $E_H$  components of the total energy density  $E_{TW} = E_C + E_H$  of semidiurnal TIW east of the Mascarene Ridge. The distance from the ridge is normalized by the wavelength of the first mode  $\lambda = 145$  km. The measurement depth is shown next to each curve.

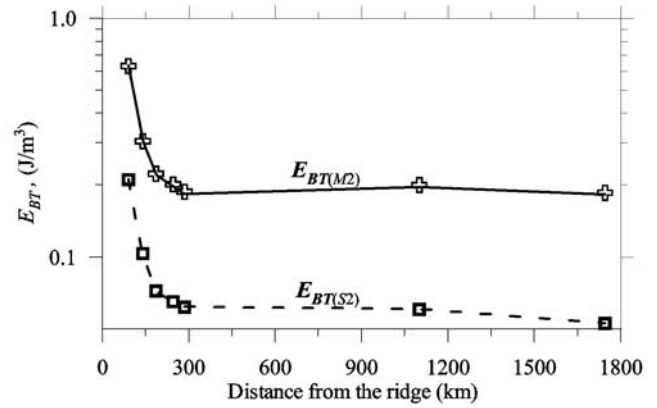


**Figure 9.** Barotropic energy density for M2 and S2 tidal constituents at various distances from the Mascarene Ridge. Fast decay of the barotropic tidal energy is confined to the first 200–250 km from the ridge.

the background energy of internal waves and only at  $x/\lambda = 12$  this contribution drops below 10% of  $E_{GM}$ .

[25] If we exclude the mooring closest to the ridge, the rest of the data ( $x/\lambda > 0.9$ ) is best fitted to an exponential function with high statistical confidence ( $r^2 = 0.9$ ). The approximation

$$E_{TW}/E_{GM} = 2.1e^{-0.3(x/\lambda)}, \quad 0.9 < x/\lambda < 12 \quad (7)$$

is shown in Figure 11 by line (b). Both equations (6) and (7) fit available data well for  $x/\lambda > 0.9$ , but the rates of TIW spatial decay are different. We do not have sufficient data to propose a conclusive decay law nor to ascertain how far from the ridge a power law is obeyed. Numerical modeling discussion in section 5 sheds some light in this regard.

[26] The energy density of the extreme amplitudes of semidiurnal TIW (section 4.1) is expected to be less sensitive to the spring-neap cycle and to mesoscale oceanic variability. A combined plot of normalized extreme

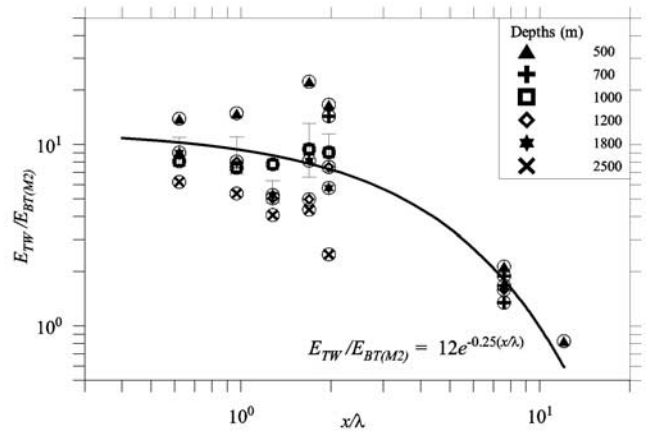


**Figure 10.** Ratio between energy densities of semidiurnal baroclinic internal tide  $E_{TW}$  and the barotropic tide  $E_{BT}$ . The dependence of  $E_{TW}/E_{BT}$  on  $x/\lambda$  is approximated by an exponential function with the coefficient of determination 0.7.

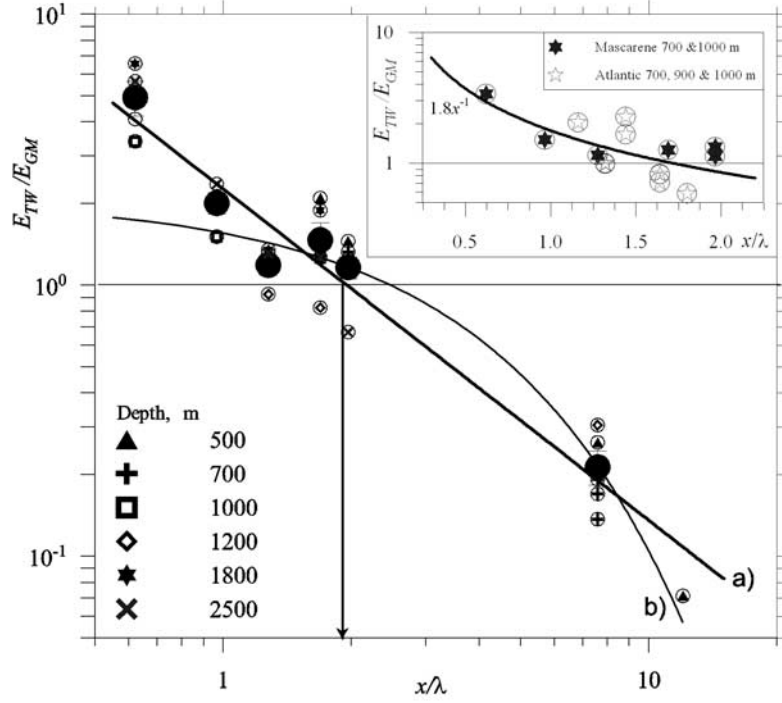


**Figure 11.** (a) Power and (b) exponential approximations for the ratio between the energy density of internal tide (Mascarene Ridge)  $E_{TW}$  (equation (3)) and the GM model energy  $E_{GM}$  (equation (5)) calculated for the region. The large dots are the mean estimates at various  $x/\lambda$ . Vertical bars show the standard errors of the mean. The data from Indian and Atlantic Oceans are shown in the inset for a limited range of  $x/\lambda$ .

TIW energies  $E_{ETW}/E_{GM}$  for the two data sets is given in Figure 12. The data collapse well to a power law

$$E_{ETW}/E_{GM} = 3(x/\lambda)^{-1.1}, \quad 0.6 < x/\lambda < 12, \quad (6')$$

indicating almost the same rate of decay as equation (6) for the mean tidal amplitudes, but with  $\sim 35\%$  higher mean level. The extreme TIW energies exceed the GM level for a longer distance, up to  $x/\lambda \approx 2.6$ . Knowledge of the intermittency of high tidal amplitude events will help obtain more accurate estimates of the averaged TIW energy. Since the extreme tidal amplitudes were defined as those that exceed 0.632 quantile of the Weibull probability distribution, extreme events are likely to occur for about 35% of the time, carrying 30–40% more energy than that deduced from the mean wave amplitude.

## 5. Comparing the Observational and Modeling Results

[27] The rate of decay of TIW energy density was investigated using an extended version of the numerical model developed by *Vlasenko* [1992]. This model has already been used to study breaking internal waves over slope topography [*Vlasenko and Hutter*, 2002] and internal tides in the Strait of Gibraltar [*Morozov et al.*, 2002].

[28] It is a nonlinear, fully nonhydrostatic, Boussinesq model for incompressible, continuously stratified, rotating ocean of variable depth. The model is essentially two dimensional ( $x-z$ ), but allows a  $x$ - and  $z$ -dependent velocity component in the  $y$  direction  $v(x, z)$  introduced by rotation

effects. The model retains all nonlinear terms and the closure is based on horizontal  $A(x)$  and vertical  $R(z)$  turbulent viscosities. Under these assumptions, the governing equations are as follows:

$$\begin{aligned} \Omega_t + J(\Omega, \Psi) - fv_z &= \frac{g\rho_x}{\rho_0} + A\Omega_{xx} + R\Omega_{zz} + (R\Psi_{zz})_z, \\ v_t + J(v, \Psi) + f\Psi_z &= Av_{xx} + (Rv_z)_z, \\ \rho_t + J(\rho, \Psi) + \frac{\rho_0 N^2(z)}{g}\Psi_x &= G\rho_{xx} + (K\rho_z)_z + (K\rho_0)_z, \end{aligned} \quad (8)$$

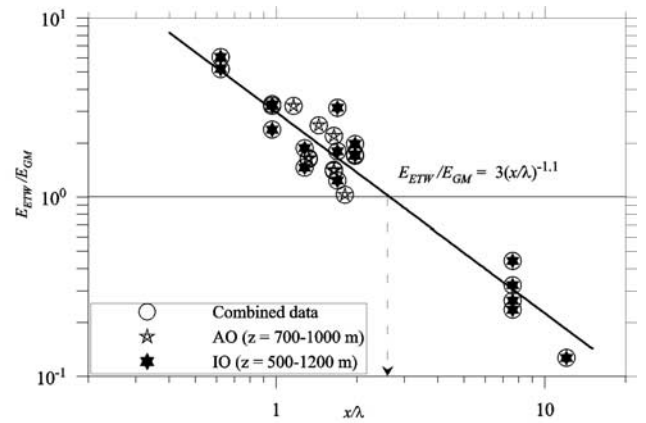


**Figure 12.** Spatial (eastward) decay of normalized energy density of the extreme tidal internal waves approximated by a power law.

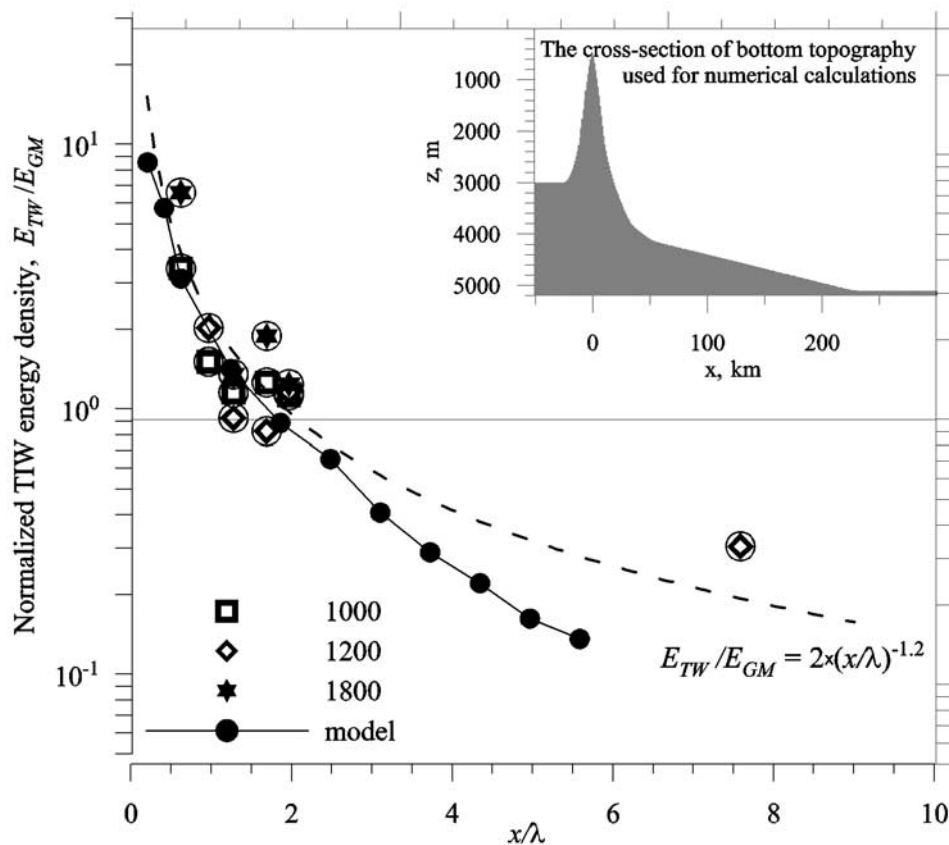


**Figure 13.** A comparison between model calculations of the TIW energy density normalized by the GM energy  $E_{GM}$  at  $z = 1200$  m (solid dots) and the observations east of Mascarene Ridge at  $z = 1000$ – $1800$  m. The geometry of the bottom relief used for calculations is in the insert.

where  $\Psi$  is the stream function ( $\Psi_z = u$ ;  $\Psi_x = -w$ );  $\Omega = \Psi_{xx} + \Psi_{zz}$  is the vorticity;  $u$ ,  $v$ , and  $w$  are the current components;  $N$  is the buoyancy frequency;  $\rho$  is the perturbation of density due to wave motion;  $\rho_0$  is the depth-dependent mean density;  $f$  is the Coriolis parameter;  $K(x)$  and  $G(x)$  are the vertical and horizontal mass diffusivities;  $J$  is the Jacobean; and  $g$  is the gravitational acceleration. The diffusivities are  $x$  dependent but not time dependent. The “rigid lid” approximation was used to model the surface boundary condition of TIW. The zero-flux boundary conditions were used at the bottom. The vorticity at the bottom was calculated as  $\Omega = \Delta\Psi$ , using the value of  $\Psi$  in the previous time step. On lateral boundaries far from the ridge, the wave perturbations of vorticity, stream function, and density are considered zero. The calculations are terminated when the wave perturbations reach the lateral boundaries. The model was forced by the oscillating stream function  $\Psi = \Psi_0 \sin \omega t$ ,  $\Psi_0$  being the amplitude at the bottom; this amplitude linearly decreases to zero at the sea surface. This forcing, which is specified by the boundary conditions for the stream function, produces a depth-independent barotropic flow with semidiurnal frequency  $\omega$ . In the case of *Morozov and Vlasenko* [1996], a simpler version of this model was used with no background rotation and vertical diffusion to predict ray trajectories of internal waves in the vicinity of the Mascarene Ridge.

[29] In the calculations, the domain with curvilinear bottom topography was transformed to a rectangular do-

main by replacing the vertical coordinate  $z$  by a new variable  $z_1$ :

$$z_1 = \frac{\int_0^z N(s) ds}{\int_0^{-H(x)} N(s) ds}.$$

Thus the grid size  $\Delta z$  depends on the stratification, referred to as sigma coordinates, allowing us to keep the number of vertical levels the same everywhere in the domain irrespective of the depth of the water column, while the layer thickness varies widely from grid point to grid point. The total number of layers was selected to be 34 in order to achieve an average vertical resolution of 150 m in the deep ocean having  $H_{\max} = 5100$  m. Far from the topography,  $\Delta z$  is the largest (500 m) at abyssal depths and smallest (20 m) in the seasonal thermocline. Closer to the topography the vertical grid size is much smaller. The sigma coordinates employed in the continuously stratified ocean considered here complement the two-layer model of *Gerkema and Zimmerman* [1995] and related studies of *Lamb* [1994] and *Hibiya et al.* [1998].

[30] An implicit finite difference numerical scheme and the method of variable directions with a second-order approximation were applied. A domain contains ridge topography with its crest at a depth of 500 m (Figure 13).

The depth of the ocean floor east of the ridge at  $x > 230$  km was set to 5100 m.

[31] The coefficients of the horizontal eddy viscosity and diffusivity were selected to be  $A = G = 250 \text{ m}^2/\text{s}$  at  $x = 0$  km gradually decreasing in sinusoidal fashion to  $200 \text{ m}^2/\text{s}$  over a distance of 100 km and constant thereafter. The vertical exchange coefficients were set at  $R = K = 10^{-2} \text{ m}^2/\text{s}$  across the entire water column over the ridge slope, and  $R = K = 10^{-4} \text{ m}^2/\text{s}$  where the bottom becomes flat. Active dynamics above the slopes of the ridge justifies greater values of the exchange coefficients therein. The amplitude of stream function of the barotropic tide was assigned  $400 \text{ m}^2/\text{s}$  at the bottom and zero at the sea surface. The calculations were run with a time step of 7.2 s and a horizontal resolution of  $\Delta x = 900$  m.

[32] The model is quite sensitive to the horizontal diffusion coefficients  $A$  and  $G$ , but it is less sensitive to vertical exchange coefficients. *Vlasenko and Hutter* [2002] and *Morozov et al.* [2002] suggested that the horizontal eddy viscosity and diffusivity in this model should be assigned the lowest possible level required for numerical stability. The set of exchange coefficients and spatial and time steps chosen for the present calculations prevented numerical instabilities that could be caused by strong nonlinearity of equation (8).

[33] The barotropic velocity components were subtracted from the model results, thus obtaining TIW-induced flow. The density oscillations were transformed into vertical isopycnal displacements using the density gradient. Both vertical displacements and horizontal velocities were band-pass filtered with the same algorithm as that used for field data processing. The model predicted  $E_{\text{TIW}}$  at  $z = 1200$  m, normalized by  $E_{\text{GM}}$ , are shown in Figure 13 (solid dots) along with the field data from the depth range 1000–1800 m. The model calculations accord reasonably with the observations for  $x/\lambda < 2-3$ , and suggest a least squared power fit indicated by the dashed line having a coefficient of determination  $r^2 = 0.83$ .

[34] The modeling results, however, deviated from the observations at some distance from the topography, showing a more rapid decrease in the energy density. It is possible that too much dissipation is imparted on the flow through subgrid modeling. Other drawbacks of the model are the assumption of a linear ridge as the TIW energy source (ignoring along-ridge variations) and representation of the ridge slope by a set of rectangular steps (the flanks of the ridge have more irregularities than can be resolved by the model). More detailed bottom relief may lead to an increase in the energy of TIW. It is also possible that the flow in the channels between the banks can generate intense TIW, as a result of which coherent wave front may not form within a few wavelengths from the ridge; this affects measurements made at the moorings.

[35] In spite of above caveats, the reasonable agreement between observations and numerical calculations within  $(2-3)\lambda$  from the topography gives credence to the estimates of spatial energy decay made in section 4.

## 6. Mixing

[36] The contribution of internal tide to the internal wave field augments energy available for vertical mixing and

dissipation in the main pycnocline. The tidal energy pathways to dissipation include wave-wave interactions, cascading of energy to smaller scales, scattering by bottom roughness elements, and reflection from sloping boundaries. According to *Müller and Xu* [1992], wave scattering is more effective than wave reflection in distributing energy from low tidal modes to higher wave numbers. This is because the relatively short time  $\tau_r$  necessary for a mode to travel back and forth between the ocean floor and sea surface, during which only about 10% of the baroclinic tidal energy can be transferred to higher modes. This conversion process becomes more inefficient as the mode number becomes higher, since  $\tau_r$  for them is much smaller, suggesting that the degeneration of TIW energy to turbulence occurs by higher modes through wave-wave interactions [*St. Laurent and Garrett*, 2002]. An exception is the possibility of reduced  $\tau_r$  for low modes in regions of exceptionally strong tidal forcing [see *Hirst*, 1991]. This implies that in the Mascarene region, where the tidal energy flux is one of the largest in the World Ocean [*Morozov*, 1995; *Kantha and Tierney*, 1997], low modes of baroclinic tide can play a substantial role in producing elevated diapycnal mixing.

[37] Theoretical [*McComas and Muller*, 1981; *Heney et al.*, 1986] as well as semiempirical [*Gregg*, 1989] models on the dissipation of internal wave energy have been tested by *Wijesekera et al.* [1993] and *Polzin et al.* [1995] against direct measurements of the kinetic energy dissipation rate  $\epsilon$  in the ocean. The measurement have been taken in regions known to comply with the GM spectrum as well as in regions such as Yermak Plateau in the eastern Arctic Ocean [CEAREX, *Wijesekera et al.*, 1993] and Canary Basin in the eastern Atlantic [NATRE, *Polzin et al.*, 1995], where the GM spectrum is not well obeyed. The theoretically deduced dissipation was in general agreement with that based on direct measurements of small-scale shear, although no one model could be identified as most suitable [*Muller et al.*, 1986]. *Polzin et al.* [1995] identified *Heney et al.*'s [1986] model as the best performing in GM regions whereas *Wijesekera et al.* [1993] preferred *McComas and Muller*'s [1981] model for non-GM regions. *Polzin et al.* [1995], however, found that NATRE data influenced by internal tide also show a closer agreement with that shown by *McComas and Muller* [1981]. Therefore we chose *McComas and Muller*'s [1981] model to obtain estimates of  $\epsilon$ , and hence to deduce turbulent diffusivities associated with degenerating TIW.

[38] *McComas and Muller* [1981] suggested parametric subharmonic instability (PSI) and induced diffusion (ID) as major nonlinear mechanisms of transferring energy among internal waves due to weak resonant interactions. A dynamic balance with stationary downscale energy flux through an inertial subrange, from energy containing to dissipation scales, was considered in their model. At low frequencies ( $f < \omega < 4f$ ), the flux is governed by PSI, which can transfer energy with frequency  $\omega_T$  to larger vertical wave numbers with frequency  $\omega_T/2$  during a characteristic timescale

$$\tau_{\text{PSI}} = (32\sqrt{10}/27\pi)\beta_*^{-2}f^{-1}N^2\hat{E}_{\text{GM}}^{-1}. \quad (9a)$$

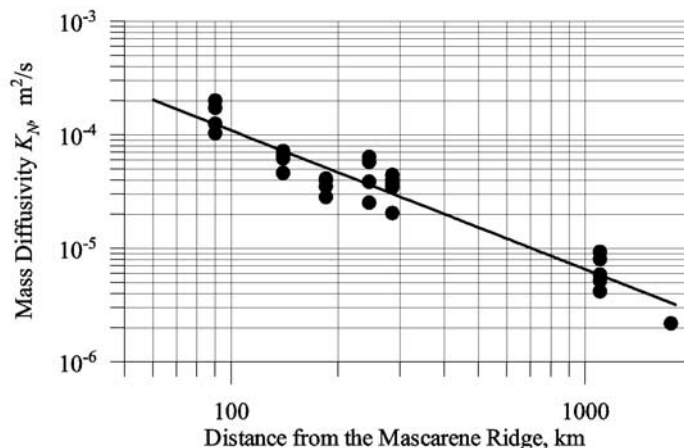


**Figure 14.** Vertical diffusivities at various distances from the Mascarene Ridge based on the dissipation estimates made using *McComas and Muller's* [1981] model.

At high frequencies ( $4f \ll \omega \ll N$ ), the flux is dominated by ID, which scatters the waves with a timescale

$$\tau_{ID} = \beta_*^{-2} f^{-1} N^2 \hat{E}_{GM}^{-1}. \quad (9b)$$

Here  $\hat{E}_{GM} = E_{GM}/\rho$  is the canonical GM energy density, where  $E_{GM}$  is given by equation (5) and  $\beta_* = j_* \pi b^{-1} N/N_o$  with the vertical mode number  $j_* = 3$  [Munk, 1981].

[39] The effectiveness of PSI in dissipating energy of semidiurnal internal tides at low latitudes was pointed out by *Olbers and Pomphrey* [1981] and *Hirst* [1991], who studied the wave-wave interactions between TIW and the internal-wave continuum [St. Laurent and Garrett, 2002]. At the mean latitude for the Mascarene Ridge (14°S), the PSI-based dissipation timescale for the semidiurnal internal tide is about 280 days for mode 1, 60 days for mode 2, and 15 days for mode 3, respectively [Olbers, 1983]. If we replace  $\hat{E}_{GM}$  in equation (10a) by the energy density  $\hat{E}_{TW} = E_{TW}/\rho$  inferred from the observations,  $\tau_{PSI}$  would range between 24 days at  $z = 500$  m and 80 days at  $z = 2500$  m. Because equations (9a) and (9b) have been derived for non-TIW, direct comparison between these estimates and those of *Olbers* [1983] is questionable, but the magnitude of numbers points to semidiurnal mode 2 as the most plausible candidate for dissipating TIW energy (by PSI) in our region of interest. The ID mechanism can work in all latitudes, causing a vertically symmetric wave field with the same energy flux going up and down at the same frequency/wave number. For this mechanism to dissipate tidal energy of low modes, it is necessary to assume that during the course of TIW propagation the energy generated near the topography is randomly redistributed over a spectrum, including at higher wave numbers.

[40] According to *Muller et al.* [1986], ID accounts for about 40% of the total energy flux. *Gregg* [1989] and *Wijesekera et al.* [1993], however, have assumed equal partition between the PSI,  $Q_{PSI}$ , and ID,  $Q_{ID}$ , energy fluxes in their calculations of  $\varepsilon_{IW}$  using

$$\varepsilon_{IW} = Q_{PSI} + Q_{ID}. \quad (10)$$

[41] We have also used equation (10) for estimating the dissipation of kinetic energy and the mass diffusivity,

$$K_N = \gamma \varepsilon_{IW} / N^2, \quad (11)$$

for the Mascarene region, replacing  $\hat{E}_{GM}$  by  $\hat{E}_{TW}$  when  $Q_{PSI} = \hat{E}_{TW}/\tau_{PSI}$  and  $Q_{ID} = \hat{E}_{TW}/\tau_{ID}$  are calculated. The mixing efficiency  $\gamma$  is assumed to have the usual value 0.2. The essential assumption here is that the energy of TIW is transferred via the inertial subrange to the dissipation scales by the mechanism suggested by *McComas and Muller* [1981] for the GM internal wave field. The quasi-stationary nature of internal tides at various distances from the topography provides some justification for this assumption.

[42] Figure 14 shows the spatial decay of  $K_N$ , from  $(1-2) \times 10^{-4}$  m<sup>2</sup>/s at  $x = 90$  km to  $2.5 \times 10^{-6}$  m<sup>2</sup>/s at  $x = 1745$  m, the latter being closer to the molecular value; the trend can be approximated by an inverse power law. Based on the GM energy density  $\hat{E}_{GM}$  (which would have been the background field in the absence of the ridge) and  $\hat{E}_{TW}$ , it can be easily shown that the ridge elevates the vertical diffusivity by a factor of 3–5 at  $x = 200-300$  km from the topography. The  $K_N$  values obtained are an order of magnitude higher than the typical value  $10^{-5}$  m<sup>2</sup>/s [Ledwell et al., 1993] observed in the main pycnocline. Between  $x = 300$  and 100 km [or  $(1-1.5)\lambda$ ], the diffusivity rises to the canonical value of  $10^{-4}$  m<sup>2</sup>/s prescribed by *Munk* [1966] in his “Abyssal Recipes.” The above estimates are in agreement with the recent proposal of *Munk and Wunsch* [1998] that there can be a significant enhancement in vertical mixing in regions conducive for the TIW generation.

## 7. Summary

[43] An investigation on the spatial decay of energy density of TIW was conducted using field data and a numerical model. Measurements were taken in the Indian Ocean east of the Mascarene Ridge and in the Canary Basin of subtropical Atlantic southeast of the Heyres-Irving-Cruiser chain of seamounts. The data allowed us to establish an approximate power law for the TIW energy decay from the source (Figure 11). The contribution of individual

processes to this decrease of energy density was not studied, though it is an important aspect.

[44] It was found that TIW lose approximately half of their energy at every wavelength  $\lambda$  of the first mode over a distance between  $x/\lambda = 0.6$  and 12 from the ridge. The role of TIW in the energetics of oceanic internal wave field becomes insignificant (less than 10% of the total GM internal wave energy) beyond about 1500–1700 km from the ridge, which is equivalent to  $(10-12)\lambda$ . Numerical calculations carried out by *Holloway and Merrifield* [1999] on the propagation of TIW away from the Hawaiian Ridge showed that the TIW energy density becomes less than that of the barotropic tide at a distance of 400 km from the source, which is approximately  $3\lambda$ . Our observations east of the Mascarene Ridge revealed a longer distance of TIW propagation ( $x = 10\lambda$ ). The dependence of the normalized energy density of TIW on distance from the topography can be approximated by a power law  $E_{\text{TIW}}/E_{\text{GM}} = 2.2 \times (x/\lambda)^{-1.2}$ , which is much faster spatial decay than that suggested by *Morozov* [1995].

[45] Numerical modeling shows that for  $x/\lambda < 2-3$  the decay of TIW energy density follows the observations, beyond which the calculated decay rate is faster. The model predicts  $E_{\text{TIW}}/E_{\text{BT}} = 1$  at  $x = 5.5\lambda$ , which is not far from that obtained by *Holloway and Merrifield* [1999]. The rapid energy decay predicted by the model can be attributed to many reasons, including the possibility that the bed roughness can serve as an additional source of internal tide generation, which is not accounted in the model. Geometric spreading is another important mechanism of energy loss. For a noncircular topography like a long ridge, however, the radial spreading is expected to be insignificant at distances much less than the characteristic length scale of the topography (which is about 1000 km in our case). This is the reason why radial spreading was neglected in our analysis.

[46] The near-field dissipation of TIW energy is a likely candidate for the observed energy loss at shorter distances from the topography. Rough estimates of vertical mixing could be made using tidal energy dissipation calculations based on the *McComas and Muller's* [1981] model, which is applicable to non-GM internal wave fields. This methodology follows *Polzin et al.* [1995] who studied the efficacy of various internal wave dissipation models for the Canary Basin (which is one of our regions of interest). Some of these models predicted a good correspondence with direct measurements of  $\epsilon$ .

[47] Mass diffusivity associated with internal tide induced diapycnal mixing was estimated to be  $K_N \approx (1-2) \times 10^{-4}$  m<sup>2</sup>/s in the main pycnocline at a distance of  $x = 100$  km from the ridge. The diffusivity decreases to  $(0.5-1.1) \times 10^{-5}$  at  $x > 1000$  km, approximately following  $x^{-1}$ . Topographically generated TIW, therefore, may lead to a significant enhancement of vertical diffusivity; for  $x < 300$  km, the diffusivity is 3–5 times the typical background value of  $10^{-5}$  m<sup>2</sup>/s of the main pycnocline.

[48] As was pointed out by a reviewer, *McComas and Muller* [1981] theory on weak wave-wave interactions based on PSI and ID mechanisms is applicable only for a random field of internal waves in the absence of vertical boundaries. Therefore its utility for ridge-generated TIW is

limited and the application of ID timescale equations (9a) and (9b) to TIW (dominated by low modes) should be done with circumspection. Following *Olbers and Pomphrey* [1981], *Hirst* [1996], and *St. Laurent and Garrett* [2002], we assumed that PSI is an effective mechanism of dissipating energy of the semidiurnal internal tides at low latitudes ( $12-14^\circ\text{S}$  for the Mascarene region) and that a vertically symmetric wave field, required for ID, can be formed some distance away from topography, permitting the use of *McComas and Muller* [1981] theory for estimating the dissipation. However, if we disregard the ID process and assign all energy dissipation to the PSI mechanism (via equation (9a)), the vertical diffusivity (Figure 14) does not increase substantially (only by 9%). Furthermore, even if topographic scattering (especially for low modes) is more important than wave-wave interactions in dissipating the TIW energy, the diffusivities are not expected to change significantly, given the low efficiency (<10%) of the former although its characteristic time process is about an order of magnitude smaller than PSI [*Müller and Xu*, 1992; *St. Laurent and Garrett*, 2002]. The problem requires more detailed observations and theoretical analysis.

## Appendix A: Mooring Measurements, Instrumentation, and Data Processing

### A1. POTOK Instrument

[49] The temperature and horizontal current components were taken by the autonomous mooring instrument POTOK. POTOK is a new generation of Russian instruments with technical characteristics far more superior than the older versions of Russian moored instruments BPV and CIITT used in the 1970s during the Polygon-70 and POLYMODE field experiments [*Saunders*, 1976; *Fomin et al.*, 1989]. The POTOK current meter is essentially based on the Aanderaa rotor-vane current meter. However, instead of a rotor, it has an impeller and instead of a single long vane it has a shorter, bivane structure. A hanger also offsets it from the mooring line, rather than hanging directly in line. This improvement of hanging at the center of hydrodynamic pressure allows positioning of the current meter in the vertical direction (CIITT instruments used in POLYMODE did not have this capability). An impeller with a horizontal axis and a vane and an internal compass are used to measure two horizontal components of the current vector. The impeller rotation measurements carried out with 9-bit resolution are integrated over a sampling interval that may vary from 56 s to 1 hour. The lower threshold of the instrument is 1 cm/s, the accuracy of current measurements is 2 cm/s, and the resolution is 1 cm/s. The vane and compass have an accuracy of  $5^\circ$  and the temperature is measured by a quartz resonator with a time constant of 30 s, an accuracy of  $0.03^\circ\text{C}$ , and a resolution of  $0.001^\circ\text{C}$ . The data are recorded on a magnetic tape or internal memory. The titanium pressure case allows reliable measurements down to 6000 m.

[50] A modern version of POTOK has been recently used in the international field experiments Nestor Neutrino [*Resvanis*, 1992] and Deep Basin [*Harkema and Weatherly*, 1996]. A report on the latter, including technical informa-

tion on POTOK, can be found on the Web page of the Florida State University, <http://www.ocean.fsu.edu>.

### A2. Mooring Stations

[51] Both surface [Fomin *et al.*, 1989] and subsurface [Demidova *et al.*, 1997; Kontar and Sokov, 1994] moorings were used in the experimental program. Each has advantages and drawbacks, depending on processes under investigation. Current measurements from the surface floats are contaminated by horizontal movements of the mooring, thus overestimating current amplitudes [SCOR Report, 1975]. Horizontal and vertical motions of surface mooring lead to erroneously high levels of energy spectra at high spectral frequencies, but tidal frequencies are almost free of this contamination [Gould *et al.*, 1974]. Temperature records are significantly less contaminated at surface floats compared to current measurements. Subsurface floats produce more contaminated temperature records compared to surface moorings. Wunsch and Dahlen [1974] showed that spectra of temperature measurements from subsurface moorings are highly correlated with those of the pressure signal due to periodic vertical oscillations of the instrument in stratified layers. The massive (2.3 t) cylindrical surface buoys with heavy anchored lines used for instrument deployments in the present study enable the restriction of such vertical oscillations to insignificant amplitudes. Goldin and Maximenko [1996] developed a mathematical model of surface buoy motion influenced by the wind stress on the float and a permanent current within the water column. Calculations based on their model show that instrument displacement in the main thermocline is within a few meters and in the upper thermocline is less than 1 m. Thus only a small amount of fictitious variance is seeped into spectra at the tidal frequency.

### A3. Demodulation of Internal Tide Components

[52] Band-pass filtering was used to demodulate semidiurnal tidal components from the time series of  $u(t)$ ,  $v(t)$ , and

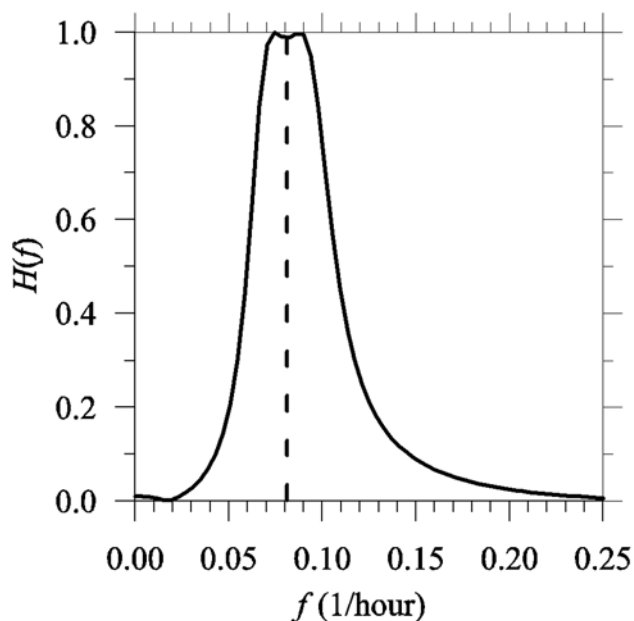


**Figure A1.** Frequency response function of the four-pole band-pass elliptic filter tuned to  $f_c = 1/12.4$  hours.

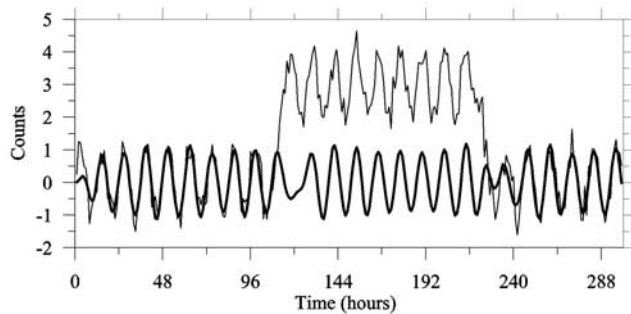


**Figure A2.** Demodulation of semidiurnal oscillations (thick line) from a simulated record (thin line) using four-pole, 40 dB band-pass elliptic filter.

$T(t)$  taken with sampling frequency  $1/3600 \text{ s}^{-1}$ . It was found that four-pole 40 dB elliptic band-pass filter [Parks and Burrus, 1987], tuned to a central frequency of  $1/12.4$  per hour with the high-low frequency cutoffs at  $1/11$  and  $1/14$  per hour, can effectively deduce the semidiurnal component. The frequency response function of this filter is given in Figure A1. An example of the demodulation of the semidiurnal component from a test record consisting of a 12.4-hour period sinusoidal oscillation of unit amplitude with superimposed random Gaussian noise is shown in Figure A2. Sharp jumps of amplitude at  $t = 110$  and  $215$  hours mimic the temperature or current meter imprints of a passing frontal zone or a mesoscale eddy. Note that the elliptic filter produces very low amplitude distortion and short-term phase shift near possible frontal zones associated with traveling eddies, meanders, or other mesoscale features. Once the signals were band-pass filtered, the vertical displacements of internal tides were calculated by dividing temperature fluctuations by the mean temperature gradient. The temperature gradients and buoyancy frequencies were obtained from temperature and density profiles. Temperature inversions were carefully excluded from the analysis.

### Notation

$E_{TW}(z) = 0.25 \left( \overline{u_{IT}^2(z)} + v_{IT}^2(z) + N^2(z) \zeta_{IT}^2(z) \right)$ $\text{and } \hat{E}_{TW} = E_{TW}/\rho$	<p>total energy (kinetic and potential) density of internal tide, <math>\text{J/m}^3</math> and <math>\text{m}^2/\text{s}^2</math>;</p> <p>amplitudes of semidiurnal internal tidal components (zonal and meridional currents) and vertical displacements, <math>\text{m/s}</math>;</p> <p>ocean of depth <math>H</math> (m) and gravity (<math>\text{m/s}^2</math>);</p>
$E_{BT} = 0.25 \rho_o [H(U_B^2 + V_B^2) + g\eta^2]/H$	<p>total energy density of barotropic tide, <math>\text{J/m}^3</math>;</p> <p>amplitudes of currents (<math>\text{m/s}</math>) and surface elevation (m) of the M2 barotropic tide;</p>
$u_{IT}, v_{IT}, \text{ and } \zeta_{IT}$	<p>depth-dependent water density (<math>\text{kg/m}^3</math>) and buoyancy frequency (<math>\text{rad/s}</math>);</p>
$H \text{ and } g$	<p>depth-dependent water density (<math>\text{kg/m}^3</math>) and buoyancy frequency (<math>\text{rad/s}</math>);</p>
$U_B, V_B, \text{ and } \eta$	<p>amplitudes of currents (<math>\text{m/s}</math>) and surface elevation (m) of the M2 barotropic tide;</p>
$\rho \text{ and } N$	<p>depth-dependent water density (<math>\text{kg/m}^3</math>) and buoyancy frequency (<math>\text{rad/s}</math>);</p>

$$E_{BTC} = 0.25 \rho_0 (U_B^2 + V_B^2)$$

$$E_{Hm}(z) = 0.25 \rho \overline{(u_{Tm}^2(z) + v_{Tm}^2(z))}$$

$$E_H = E_{Hm} - E_{BTC}$$

$$= 0.25 \rho \overline{(u_{IT}^2(z) + v_{IT}^2(z))}$$

$$E_c = 0.25 \rho N^2 \overline{\zeta_{IT}^2(z)}$$

$$E_0 = E_{Hm} + E_c$$

$$E_{ETW}$$

$$E_{GM} = \rho b^2 N_0 N E$$

$$\text{and } \dot{E}_{GM} = E_{GM} / \rho$$

$b = 1.3 \text{ km}, E = 6.3 \times 10^{-5},$   
 $N_0 = 5.3 \times 10^{-3} \text{ s}^{-1}$

energy of barotropic currents,  $\text{J/m}^3$ ;  
total measured horizontal energy density,  $\text{J/m}^3$ ;  
semidiurnal tidal components obtained from mooring current series (m/s);  
horizontal kinetic energy density of internal tide,  $\text{J/m}^3$ ;  
potential energy density of internal tide,  $\text{J/m}^3$ ;  
total energy density at the semidiurnal frequency,  $\text{J/m}^3$ ;  
“extreme” energy density of internal tide calculated based on the TIW amplitudes, which exceeds a threshold level of probability of 0.63,  $\text{J/m}^3$ ;  
total energy density in the GM internal wave field model,  $\text{J/m}^3$  and  $\text{m}^2/\text{s}^2$ ;  
parameters of the GM model.

Heney, F. S., J. Write, and S. M. Flatte, Energy and action flow through the internal wave field: An eikonal approach, *J. Geophys. Res.*, *91*, 8487–8495, 1986.

Hibiya, T., M. Ogasawara, and Y. Niwa, A numerical study of the fortnightly modulation of basin-ocean water exchange across a tidal mixing zone, *J. Phys. Oceanogr.*, *28*, 1224–1235, 1998.

Hirst, E., Internal wave-wave resonance theory: Fundamentals and limitations, in *Dynamics of Oceanic Internal Gravity Waves: Proceedings of ‘Aha Huliko’ a Hawaiian Winter Workshop*, edited by P. Muller and D. Henderson, pp. 211–226, School of Ocean and Earth Sci. and Technol., Univ. of Hawai‘i at Manoa, Honolulu, 1991.

Holloway, P. E., and M. Merrifield, Internal tide generation by seamounts, ridges and islands, *J. Geophys. Res.*, *104*(C11), 25,937–25,951, 1999.

Inall, M. E., T. P. Ripperth, and T. J. Sherwin, Impact of nonlinear waves on the dissipation of internal tidal energy at a shelf break, *J. Geophys. Res.*, *105*(C4), 8687–8705, 2000.

Kantha, L. H., and C. C. Tierney, Global baroclinic tides, *Prog. Oceanogr.*, *40*, 163–188, 1997.

Kontar, E. A., and A. V. Sokov, A benthic storm in the northeastern tropical Pacific over the fields of manganese nodules, *Deep Sea Res.*, *41*, 1069–1089, 1994.

Lamb, K. G., Numerical experiments of internal wave generation by strong tidal flow across a finite amplitude bank edge, *J. Geophys. Res.*, *99*, 843–864, 1994.

Ledwell, J. R., A. J. Watson, and C. S. Law, Evidence for slow mixing across the pycnocline from an open-ocean tracer-released experiment, *Nature*, *364*, 701–703, 1993.

Lozovatsky, I. D., and A. Y. Erofeev, Statistical approach to eddy viscosity simulation for numerical models of the upper turbulent oceanic layer, *J. Mar. Syst.*, *4*(5), 391–399, 1993.

McComas, C. H., and P. Muller, The dynamic balance of internal waves, *J. Phys. Oceanogr.*, *11*, 970–986, 1981.

Merrifield, M. A., P. E. Holloway, and T. S. Johnston, The generation of internal tides at the Hawaiian Ridge, *Geophys. Res. Lett.*, *28*(4), 559–562, 2001.

Morozov, E. G., Semidiurnal internal wave global field, *Deep Sea Res.*, *42*, 135–148, 1995.

Morozov, E. G., and V. I. Vlasenko, Extreme tidal internal waves near the Mascarene Ridge, *J. Mar. Syst.*, *9*(3–4), 203–210, 1996.

Morozov, E. G., V. I. Vlasenko, T. A. Demidova, and V. V. Ledenev, Tidal internal wave propagation over large distances in the Indian Ocean, *Oceanology*, *39*, 42–46, 1999.

Morozov, E. G., K. Trulsen, M. G. Velarde, and V. I. Vlasenko, Internal tides in the Strait of Gibraltar, *J. Phys. Oceanogr.*, *32*, 3193–3206, 2002.

Müller, P., and N. Xu, Scattering of oceanic internal waves off random bottom topography, *J. Phys. Oceanogr.*, *22*, 474–488, 1992.

Muller, P., G. Holloway, F. Heney, and N. Pomphrey, Nonlinear interactions among internal gravity waves, *Rev. Geophys.*, *24*, 493–536, 1986.

Munk, W. H., Abyssal recipes, *Deep Sea Res.*, *13*, 707–730, 1966.

Munk, W. H., Internal waves and small scale processes, in *Evolution of Physical Oceanography*, edited by B. A. Warren and C. Wunsch, pp. 264–291, MIT Press, Cambridge, Mass., 1981.

Munk, W. H., and C. Wunsch, Abyssal recipes: II. Energetics of tidal and wind mixing, *Deep Sea Res.*, *45*, 1977–2010, 1998.

New, A. L., Internal tidal mixing in Bay of Biscay, *Deep Sea Res.*, *35*, 691–709, 1988.

Olbers, D. J., Models of the oceanic internal wave field, *Rev. Geophys.*, *21*, 1567–1606, 1983.

Olbers, D. J., and N. Pomphrey, Disqualifying two candidates for the energy balance of oceanic internal waves, *J. Phys. Oceanogr.*, *11*, 1423–1425, 1981.

Parks, T. W., and C. S. Burrus, *Digital Filter Design*, 342 pp., John Wiley, New York, 1987.

Polzin, K., J. M. Tool, and R. Schmitt, Finescale parameterization of turbulent dissipation, *J. Phys. Oceanogr.*, *25*, 306–328, 1995.

Resvanis, L. K., (Ed.), *Second NESTOR International Workshop, Pylos, Greece*, 413 pp., Nestor Inst. for Deep Sea Res., Technol. And Neutrino Astroparticle Phys., Pylos, Greece, 1992.

Saunders, P. M., Near surface current measurements, *Deep Sea Res.*, *23*, 249–257, 1976.

SCOR, Working Group 21, An intercomparison of some current meters, *UNESCO Tech. Pap. Mar. Sci.*, *17*, 43 pp., 1975.

Sjoberg, B., and A. Stigebrandt, Computation of the geographical distribution of the energy flux to mixing processes via internal tides and the associated vertical circulation in the oceans, *Deep Sea Res.*, *39*, 269–291, 1992.

[53] **Acknowledgments.** The work was supported by the U.S. Office of Naval Research, grant N00014-97-1-0140. Authors are indebted to V. Vlasenko (Institute of Mechanics, Technical University Darmstadt, Germany) for his expertise with the numerical model and to S. Erofeeva (Oregon State University) for the calculations of barotropic tidal constituents near the Mascarene Ridge and the chain of seamounts in the Canary Basin using the OTIS software. This paper was significantly improved by the useful comments and recommendations made by two anonymous reviewers.

## References

Barber, N. F., The directional resolving power of an array of wave detectors, in *Ocean Wave Spectra*, pp. 137–150, Prentice-Hall, Old Tappan, N. J., 1963.

Demidova, T. A., S. A. Kovachev, and A. V. Sonkin, Property of noise registered by pop-up oceanic bottom seismograph, *J. Atmos. Oceanic Technol.*, *14*, 883–888, 1997.

Dushaw, B. D., B. D. Cornuelle, P. F. Worcester, B. W. Howe, and D. S. Luther, Barotropic and baroclinic tides in the central North Pacific Ocean determined from long-range reciprocal acoustic transmissions, *J. Phys. Oceanogr.*, *25*, 631–647, 1995.

Egbert, G. D., Tidal data inversion: Interpolation and inference, *Prog. Oceanogr.*, *40*, 53–80, 1997.

Egbert, G. D., and S. Erofeeva, Efficient inverse modeling of barotropic ocean tides, *J. Atmos. Oceanic Technol.*, *19*, 183–204, 2002.

Fomin, L. M., V. M. Kushnir, and V. B. Titov, *Measurements of Ocean Currents*, 197 pp., Nauka, Moscow, 1989.

Gerkema, T., and J. T. F. Zimmerman, Generation of nonlinear internal tides and solitary waves, *J. Phys. Oceanogr.*, *25*, 1081–1098, 1995.

Goldin, A. Y., and N. A. Maximenko, Application of mathematical model to the analysis of measured temperature distortion, *Oceanology*, *36*, 939–945, 1996.

Gould, W. J., W. J. Schmitz, and C. Wunsch, Preliminary field results for a Mid-Ocean Dynamic Experiment (MODE-0), *Deep Sea Res.*, *21*, 911–933, 1974.

Gregg, M. C., Scaling turbulent dissipation in the thermocline, *J. Geophys. Res.*, *94*(C7), 9686–9698, 1989.

Harkema, R., and G. L. Weatherly, A compilation of moored current meter data from the southern boundary of the Brazil Basin for the Deep Basin experiment September 1993–March 1995, *Tech. Rep. CMF-96-01*, Fla. State Univ., Tallahassee, June 1996.

- St. Laurent, L., and C. Garrett, The role of internal tides in mixing the deep ocean, *J. Phys. Oceanogr.*, 32, 2882–2899, 2002.
- Thorpe, S. A., Fronts formed by obliquely reflecting internal waves at a sloping boundary, *J. Phys. Oceanogr.*, 29, 2462–2467, 1999.
- Torgimson, G. M., and B. M. Hickey, Barotropic and baroclinic tides over the continental slope and shelf off Oregon, *J. Phys. Oceanogr.*, 9, 945–961, 1979.
- Vlasenko, V. I., Nonlinear model for the generation of baroclinic tides over extensive inhomogeneities of the seabed relief, *Sov. J. Phys. Oceanogr.*, 3, 417–424, 1992.
- Vlasenko, V. I., and K. Hutter, Numerical experiments on the breaking of solitary internal waves over a slope-shelf topography, *J. Phys. Oceanogr.*, 32, 1779–1793, 2002.
- Weibull, W., A statistical distribution function of wide applicability, *J. Appl. Mech.*, 9, 293–297, 1951.
- Wijesekera, H., L. Padman, T. Dillon, M. Levine, and C. Paulson, The application of internal-wave dissipation models to a region of strong mixing, *J. Phys. Oceanogr.*, 23, 269–286, 1993.
- Wunsch, C., and J. Dahlen, A moored temperature and pressure recorder, *Deep Sea Res.*, 21, 145–154, 1974.
- 
- H. J. S. Fernando and I. D. Lozovsky, Environmental Fluid Dynamics Program, Department of Mechanical and Aerospace Engineering, Arizona State University, Tempe, AZ 85287-9809, USA. (j.Fernando@asu.edu; i.lozovsky@asu.edu)
- E. G. Morozov, P. P. Shirshov Institute of Oceanology, Russian Academy of Sciences, Moscow 117851, Russia. (emorozov@mtu-net.ru)